drones

MDPI

Article

Design and Experimental Study on an Innovative UAV-LiDAR Topographic Mapping System for Precision Land Levelling

Mengmeng Du [1]*, Hanyuan Li [2], and Ali Roshanianfard [3]

[1] College of Agricultural Equipment Engineering, Henan University of Science and Technology, 471003, Luoyang, China; dualmon.du@haust.edu.cn
[2] College of Agricultural Equipment Engineering, Henan University of Science and Technology, 471003, Luoyang, China; 200320041519@stu.haust.edu.cn
[3] Department of Agriculture and Natural Resources, University of Mohaghegh Ardabili, 566199, Iran; alirf@uma.ac.ir
* Correspondence: dualmon.du@haust.edu.cn

Abstract: Topographic maps provide detailed information on variations of ground elevation, which are essential to precision farmland levelling. This paper reports the development and experimental study on an innovative approach of generating topographic maps at farmland-level with advantages of high efficiency and simplicity of implementation. The experiment uses a low-altitude Unmanned Aerial Vehicle (UAV) as a platform and integrates Light Detection and Ranging (LiDAR) distance measurements with Post Processing Kinematic Global Positioning System (PPK-GPS) coordinates. Topographic mapping experiment was conducted over 2 fields in Henan province, China, and primitive errors of the topographic surveying data were evaluated. Root Mean Square Error (RMSE) between elevation data of the UAV-LiDAR topographic mapping system and ground truth data was calculated as 4.1 cm and 3.6 cm for field 1 and field 2, respectively, which proved the feasibility and high accuracy of the topographic mapping system. Furthermore, accuracies of topographic maps by using different geo-spatial interpolation models were also evaluated. The results showed that TIN (Triangulated Irregular Network) interpolation model expressed best performances for both field 1 with sparse topographic surveying points and field 2 with relatively dense topographic surveying points, when compared with other interpolation models. Besides, we concluded that as the spatial resolution of topographic surveying points is intensified from 5 m×0.5 m to 2.5 m×0.5 m, the accuracy of topographic map based on TIN model improves drastically from 7.7 cm to 4.6 cm. Cut-fill analysis is also implemented based on topographic maps of TIN interpolation model. The result indicated that the UAV-LiDAR topographic mapping system could be successfully used to generate topographic maps with high accuracy, which could provide instructive information for precision farmland levelling.

Keywords: Topographic map; Agricultural remote sensing; Unmanned aerial vehicle; Light detection and ranging; Interpolation model

Citation: To be added by editorial staff during production.

Academic Editor: Firstname Lastname

Received: date
Accepted: date
Published: date

Publisher's Note: MDPI stays neutral with regard to jurisdictional claims in published maps and institutional affiliations.

Copyright: © 2022 by the authors. Submitted for possible open access publication under the terms and conditions of the Creative Commons Attribution (CC BY) license (https://creativecommons.org/licenses/by/4.0/).

1. Introduction

Surface unevenness of farmlands has been pointed out as a major issue that affected agricultural drainage efficiency. Hu et al. (2014) reported that over 20% of irrigation water could be wasted due to rough land surface of paddy fields, and Rickman (2002) concluded that unleveled rice fields suffered about 24% yield loss on average when compared to the effectively leveled ones for the same rice variety and the same fertilizer input [1],[2]. As precision farmland levelling facilitates agricultural drainage, improves crop establishment, and increases crop yield, many researchers both in academia and industry have proposed different methodologies on removing mounds and puddles inside farmland [3],[4]. Generally, two major precision farmland levelling techniques could be

enumerated: laser farmland levelling and GPS (Global Positioning System) farmland levelling [5]. And accurate topographic map is essential to precision farmland levelling, which refers to a 2D (two-dimensional) graphic representation of a terrestrial land surface feature using contour lines, hypsometric tints, and relief shading[6]-[9]. As for the laser farmland leveler, selection of preset height of laser transmitter directly determines cutting depth of each point, i.e., cut-fill ratios. Without referring to an accurate topographic map it is almost impossible to manually set an appropriate height for the laser transmitter efficiently and accurately, in order to optimize volumes of the relocated earth. It is not unusual that the scraper of land leveler hangs too high to cut very few soils, or worse, tractor gets stuck and cannot move forward due to high slipping rate when the scraper cuts too deep. On the other hand, GPS farmland leveler measures and adjusts height of scraper by comparing current height of the GPS receiver module with the reference height plane to complete earth-moving process, which also needs an accurate topographic map to form the reference height plane. In thus, accuracy, efficiency, as well as energy consumption of precision farmland levelling is in high accordance with the delicacy of farmland topographic maps [9].

To generate topographic maps, new technologies including terrestrial laser scanning, aerial photogrammetry and airborne laser scanning are recently utilized for civil construction survey, urban ecology modeling, forest monitoring, and etc. [10]-[17], while theodolite, total station, and handhold RTK (Real Time Kinematic) - GPS module remain the conventional and primary tools used in common topographic surveys[18]-[22]. Topographic survey using handhold GPS module or tripod-based total station is featured with low efficiency, which cannot be applied into large-area operations. On the other hand, topographic survey in remote sensing manner covers large areas and is capable of obtaining adequate data, in spite of high cost and complicated calibration procedures. Corsini et al. (2013) monitored and mapped a slow-moving compound rock slide by integration of airborne laser scanner, terrestrial laser scanner, and automated total station, which quantified slope movement in the order of centimeters to a few decimeters[23]. Pablo et al. (2017) evaluated a mobile LiDAR (Light Detection and Ranging) system mounted on a car to develop an architectural analysis by generating 3D point cloud[24]. Terrone et al. (2021) identified manmade landforms and assessed morphological evolution of the city of Genoa by coupling historical maps and LiDAR data[25]. There are also plenty of research works and products providing DSM based on airborne photogrammetry or satellite stereo-imagery [26]-[33]. However, processing aerial images to generate photogrammetric DSM (Digital Surface Model) usually needs strict camera calibration and a large number of well spatially-distributed GCPs (Ground Control Points), which in photogrammetry or computer vision domain refers to such features that are easily recognizable and distinguishable in both the reality world and the images. The spatial resolution as well as accuracy of such topographic maps usually reaches several decimeters to tens of meters, which cannot meet high requirements of topographic maps with centimeter-level accuracy for precision farmland levelling.

Therefore, in this study we developed and experimentally evaluated an innovative topographic mapping system for precision farmland levelling, which is based on a low-altitude UAV (Unmanned Aerial Vehicle). The UAV is equipped with LiDAR device and PPK (Post Processing Kinematic)-GPS modules, which are utilized to conduct topographic survey in a simple and totally autonomous manner. This research integrates multi-source remote sensing data onboard the UAV platform, including LiDAR distance measurements, attitude information (pitch and roll) of the UAV's flight controller, and PPK-GPS positioning data (latitude, longitude, altitude). And the ultimate objective is to generate topographic maps of farmlands with centimeter-level accuracy efficiently both in time and cost, by using geo-spatial interpolation models.

2. Materials and Methods

2.1 Experiment equipment

Farmland topographic mapping experiment was established over 2 fields located in Kaifeng City, Henan Province, China. Each field accounts for about 1 500 m² and 1 200 m², respectively, shown in **Figure 1** as field 1 and field 2. Previous crop was maize, and weeds inside the fallow fields were manually removed prior to the experiment, so that there were no significant foreign attachments on ground surface.

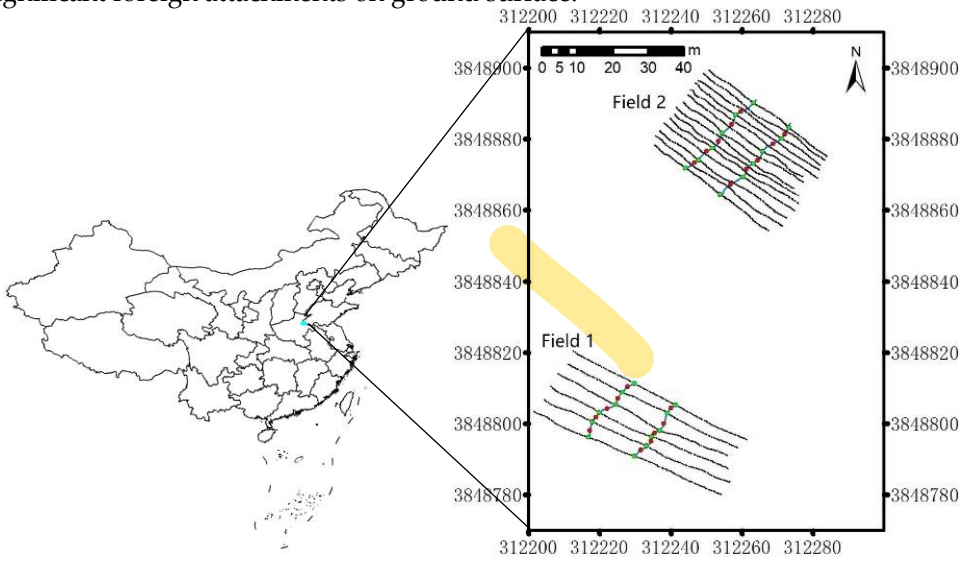


Figure 1 . Flight path of UAV-LiDAR topographic surveying experiment and locations of accuracy validating points.

A hexa-copter (TIANTU UAV Co., Ltd, Beijing, China) was used as the UAV platform, shown in **Figure 2 (a)**. High accuracy LiDAR distance measuring device (JENOPTIK, Jena, Germany) was used to measure the distance between UAV-LiDAR topographic mapping system and ground surface, which was rigidly fixed under the UAV platform pointing vertically downwards. 2 GPS modules were used to calculate 3D positioning coordinates at the frequency of 10 Hz of the UAV-LiDAR topographic mapping system in the PPK manner. One GPS module was installed on the top of the UAV as a rover receiver, while the other was fixed nearby the field as a base receiver, also shown in **Figure 2 (b)**.



(a) UAV platform (b) Base receiver of PPK-GPS module

Figure 2. Equipment of topographic surveying experiment.

Autonomous UAV flight was conducted on 24th October 2020, using flight paths designed beforehand at the speed of about 5 m/s and altitude of about 30 m above ground level. Trajectories of 2 autonomous flights over the experimental fields are shown in **Figure 1**, and cross-track interval of field 1 and field 2 was set as about 5 m and 2.5 m, respectively. From the flight speed, positioning frequency of GPS module, and cross-track

interval, spatial resolution of the topographic surveying data for field 1 and field 2 was calculated as about 5 m×0.5 m and 2.5 m×0.5 m.

2.2 Acquiring PPK-GPS coordinates

Theoretically, standalone GPS receiver usually has a positioning accuracy varying from submeter to several meters[34],[35]. On the other hand, RTK-GPS module uses a network of ground or virtual reference stations to rectify GPS rover receiver's positioning data, and its positioning accuracy could be significantly improved up to about 2~5 centimeters. But as RTK-GPS device is embedded with communication modules for data transmission via radio signal or cellular network, it is always too large in size and/or weight to be installed upon small-sized UAV. Therefore, in this study two identical light-weight PPK-GPS modules were used to collect high-accuracy positioning data in the same manner with the RTK-GPS module, except that there is no data link in real-time between these two GPS modules. After the completion of UAV topographic mapping flight, GPS positioning data of rover receiver as well as base receiver were acquired, respectively; and we could dynamically rectify GPS rover receiver's positioning data in the post-processing style with the reference of GPS base receiver's positioning data in the following manner.

Firstly, both GPS base and rover receiver were held stationary before the UAV platform took off for over 30 minutes consecutively, and therefore 18 000 sets of effective static positioning data of each GPS module at the frequency of 10 Hz were obtained. Horizontal positioning data of the stationary GPS base receiver were shown in **Figure 3(a)**, from which we may see that horizontal positioning accuracy of standalone GPS module is about 3 m. By using arithmetic averaging method, the reference coordinate (x_r, y_r, h_r) for PPK-GPS algorithm was calculated out of GPS base receiver's positioning data$(x_{basei}, y_{basei}, h_{basei})$ as (3848750.598E, 312414.385N, 63.754m), according to **Equation (1) ~ (3)**.

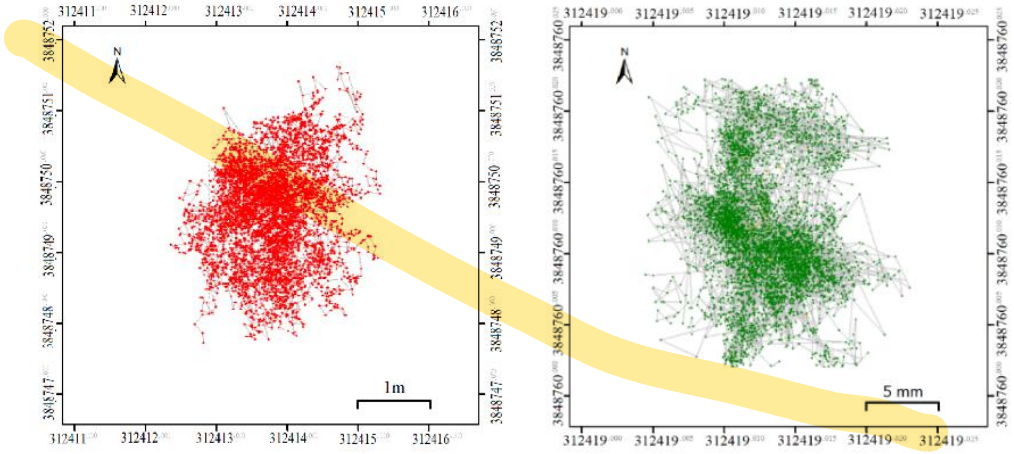
$$x_r = \sum_{i=1}^{18000} \frac{x_{basei}}{18000} \quad (1)$$

$$y_r = \sum_{i=1}^{18000} \frac{y_{basei}}{18000} \quad (2)$$

$$h_r = \sum_{i=1}^{18000} \frac{h_{basei}}{18000} \quad (3)$$

where x_r, y_r, and h_r refers to easting, northing, and altitude of the reference coordinate for the PPK algorithm, while x_{basei}, y_{basei}, and h_{basei} refers to easting, northing, and altitude of the positioning data of GPS base receiver, respectively.

Subsequently, positioning data of GPS rover receiver $(x_{rovi}, y_{rovi}, h_{rovi})$ as well as base receiver over the same period were processed in RTKLIB development environment by using PPK-GPS algorithm, where x_{rovi}, y_{rovi}, and h_{rovi} refers to easting, northing, and altitude of positioning data of the GPS rover receiver, respectively. PPK-GPS algorithm calculates position deviations between each positioning data of GPS base receiver $(x_{basei}, y_{basei}, h_{basei})$ and the reference coordinate (x_r, y_r, h_r) based on carrier phase analysis. It then uses the deviation information to rectify the corresponsive positioning data of GPS rover receiver $(x_{rovi}, y_{rovi}, h_{rovi})$. Thus, PPK-GPS positioning data were acquired as $(x_{GPSi}, y_{GPSi}, h_{GPSi})$, where x_{GPSi}, y_{GPSi}, and h_{GPSi} refers to easting, northing, and altitude of the PPK-GPS positioning data, respectively.

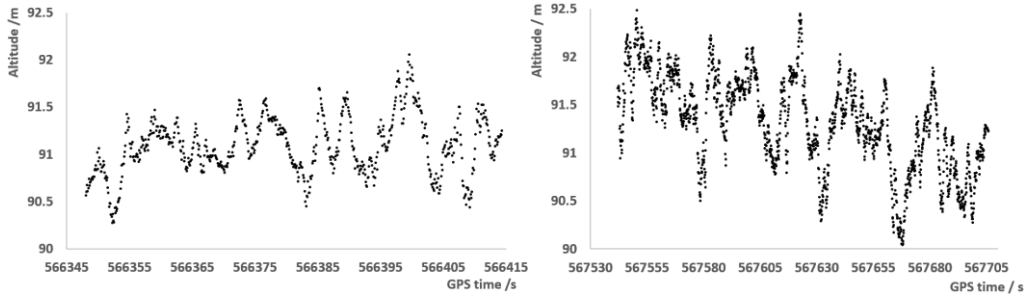


(a) standalone GPS (b) PPK-GPS

Figure 3. Positioning accuracy of standalone GPS and PPK-GPS.

The horizontal PPK-GPS positioning data of the stationary GPS rover receiver were also shown in **Figure 3(b)**, from which we may conclude that the horizontal positioning accuracy of PPK-GPS module is about 2 cm. The comparison of static positioning accuracy of standalone GPS and PPK-GPS shown in **Figure 3** clearly indicates that PPK-GPS positioning data have high accuracy and is capable of precisely measuring 3D coordinates of the UAV-LiDAR topographic mapping system.

Finally, GPS base receiver was kept at the same location, and GPS rover receiver onboard the UAV platform was used to conduct topographic mapping experiment. The UAV flight lasted for about 12 minutes for each field, and totally 675 and 1 626 set of PPK-GPS positioning data were obtained for field 1 and field 2, respectively, after removing noise data during taking-off, landing, and turning-around. The horizontal positioning coordinates of PPK-GPS data were already shown in **Figure 1**, while altitudes of PPK-GPS data were shown in **Figure 4.** From **Figure 4** we may observe the variations of UAV's flight altitude from 90 m to 92.5 m, which is caused by its intrinsic aerodynamic factors and influence of turbulence.



(a) field 1 (b)field 2

Figure 4. Altitudes of PPK-GPS positioning data onboard the UAV platform.

2.3 Rectify LiDAR distance measurements by using UAV's attitude information

LiDAR is based on time-of-flight principle and has a measuring range up to 300 m and 1 mm measuring resolution at the frequency of 2000 Hz[36]-[39]. The laser beam divergence of the LiDAR distance measurement device is 1.7 milliradians, and the spatial coverage of each measurement is about 60 mm×20 mm from a distance of about 30 m, shown in **Figure 5**. A mini-computer (GB-XMI1-3537, Gigabyte, China) is connected with the LiDAR through a universal serial bus cable, which saves each distance measurement onboard in real time. As output frequency of PPK-GPS's positioning data is 10 Hz, a mean filter with 200 step-size was applied to raw LiDAR distance measurements. In thus, the output frequency of LiDAR distance measurements was altered from 2000 Hz to 10 Hz,

in order to align multi-sources remote sensing data according to time sequences and also improve LiDAR distance measuring accuracy in the meantime. Due to aerodynamic characteristics, UAV body is apt to tilt irregularly during cruise flight. Because electronical gimbals cannot meet the real-time stabilizing requirements in this study, LiDAR was rigidly fixed below the UAV platform and UAV's attitude information were used to compensate such influences like vibration and air disturbance during flight.

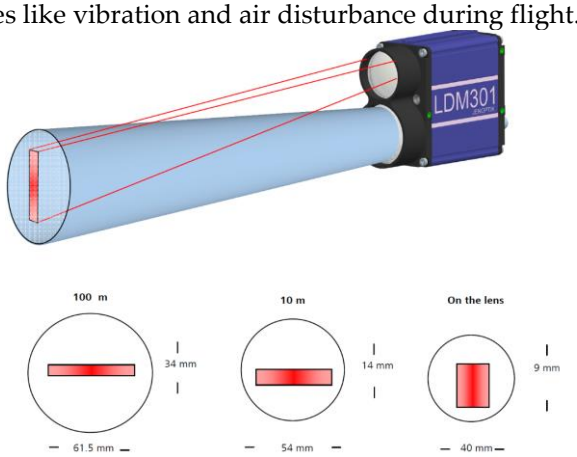


Figure 5. Spatial coverage of LiDAR distance measurement.

Attitude of UAV is usually described by means of Euler angles defined as pitch (θ), roll (ϕ), and yaw (ψ) [40]-[42]. In this study we utilize an extended Kalman filter to integrate data from multiple sensors of MEMS (Micro-Electro-Mechanical System) gyroscope, accelerometer, and magnetometer for attitude estimation. Gyroscope is an inertial sensor for measuring orientation based on angular momentum principles, and tri-axial angles $\left[\theta_{gyro}\ \phi_{gyro}\ \psi_{gyro}\right]^{\mathrm{T}}$ can be acquired by integral operation, expressed in **Equation (4)**. However, due to temperature variations of gyroscope, errors accumulate along with time and accuracy of MEMS gyroscope's attitude data would be compromised. On the other hand, accelerometer was used to measure UAV's orientation based on trigonometric functions of the acceleration of gravity components in each axial, expressed in **Equation (5)** and **Equation (6)**. MEMS magnetometer is also used for precisely calculating change of UAV's heading yaw based on magnetic intensity components in each axial $[m_x, m_y, m_z]^T$, in combination with measurements of gyroscope and accelerometer[43],[44].

$$\left[\theta_{gyro}\ \phi_{gyro}\ \psi_{gyro}\right]^T = \int\left[\omega_x\ \omega_y\ \omega_z\right]^T dt \quad (4)$$

where $\theta_{gyro}, \phi_{gyro,}$ and ψ_{gyro} is pitch, roll, and yaw of UAV platform from gyroscope, respectively; while $\omega_x, \omega_y,$ and ω_z is raw rotation rate (degree/s) of each axial from gyroscope.

$$\theta_{acce} = -arcsin\left(\frac{g_x}{\sqrt{g_x^2+g_y^2+g_z^2}}\right) \quad (5)$$

$$\phi_{acce} = arctan\left(\frac{g_y}{g_z}\right) \quad (6)$$

where θ_{acce} and ϕ_{acce} is pitch and roll of UAV from accelerometer, respectively; while g_x, g_y, and g_z is acceleration components readings in each axial from the accelerometer.

Therefore, in order to further improve accuracy of LiDAR distance measurements, attitude data (pitch θ_i and roll φ_i) of UAV platform were used to get nadir distance, according to **Equation (7)**. Nadir is defined as the angle that points directly downward, or 0° from the luminaire, shown in **Figure 6.** Variations of nadir distance between the LiDAR device and ground surface during the UAV-LiDAR topographic surveying process were shown in **Figure 7,** from which we may conclude that the nadir distance between the UAV-LiDAR system and ground surface varies from 25.5 m to 28.5 m for both field 1 and field 2. The variations of nadir distance between the UAV-LiDAR topographic mapping

system and ground surface arise from many factors, such as the ever-changing altitude of the UAV platform during flight and the field terrain itself.

$$d_{ni} = d_i \times \cos\theta_i \times \cos\varphi_i \quad (7)$$

where d_{ni} and d_i is the nadir distance and the actually measured distance between the LiDAR device and ground surface, while θ_i and φ_i is the attitude angle of pitch and roll of the UAV flight controller, respectively.

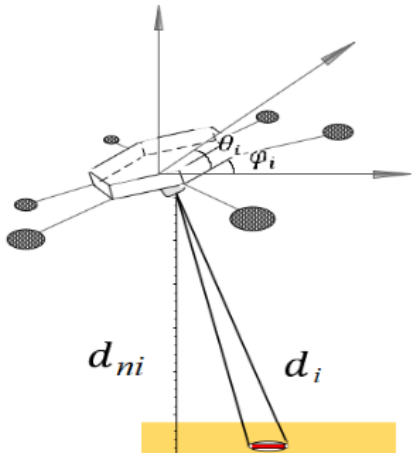
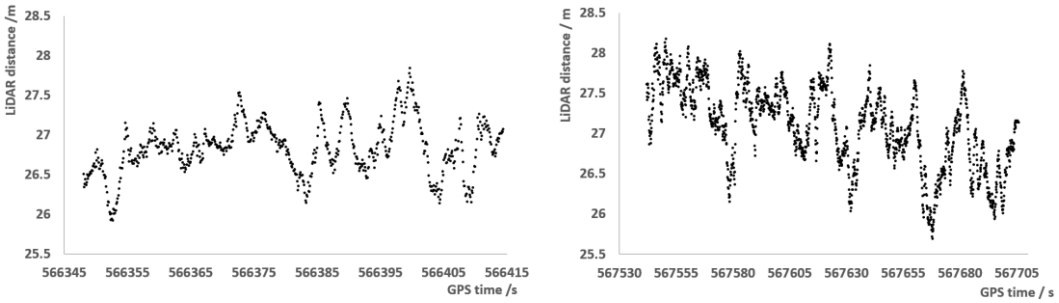


Figure 6. Scheme of rectifying LiDAR distance measurements by using UAV's attitude information.



(a) Field 1 (b) Field 2

Figure 7. Nadir distance between the UAV-LiDAR system and ground surface.

3. Results and discussion

3.1 Acquiring 3D coordinates of ground surveying points

Scheme of calculating elevation of ground surveying points (h_i) is elaborated in **Figure 9**, which could be calculated according to **Equation (8)**. Subsequently, by replacing h_{GPSi} with h_i, 3D coordinates of ground surveying points could be obtained as $(x_{GPSi}, y_{GPSi}, h_i)$.

$$h_i = h_{GPSi} - h_{fix} - d_{ni} \quad (8)$$

where h_i, h_{GPSi}, h_{fix} and d_{ni} is the elevation of ground surveying points, the altitude of UAV's PPK-GPS coordinates, the installation height difference between the GPS rover receiver and the LiDAR device (0.66 m), and the nadir distance between the UAV-LiDAR system and ground surface, respectively.

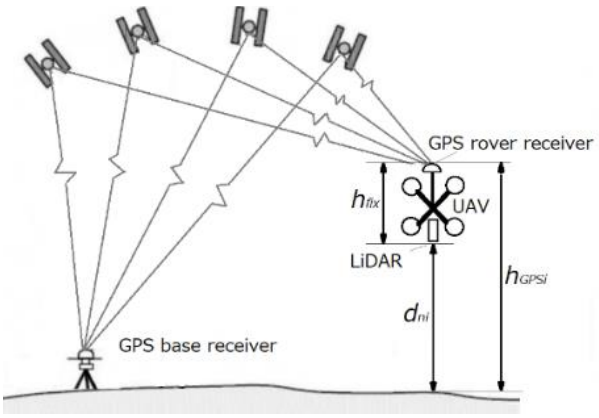
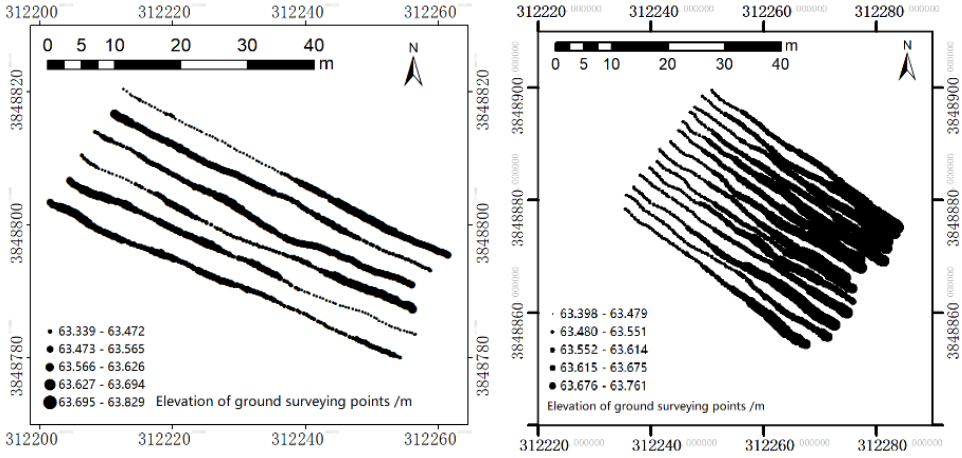


Figure 8. Scheme of calculating elevations of ground surveying points.

Based on 3D coordinates of each topographic surveying point, topographic maps indicating spatial variations of within-field ground elevation were generated by using ArcMap (ESRI Inc., Redlands, AB, Canada), shown in **Figure 9**. From the graduated symbols representing different levels of ground elevation, we can visually specify concave features (puddles) at each end for field 1, and understand the general high-south-low-north terrain for field 2, with ground elevations varying from 63.339 m to 63.829 m and 63.398 m to 63.761 m, respectively.



(a) Field 1 (b) Field 2

Figure 9. Graduated symbols represent elevations of ground surveying points.

3.2 Generating topographic maps based on interpolation models

In this study, we used 675 and 1626 set of effective topographic mapping data for field 1 and field 2, respectively, to generate topographic maps based on different interpolation models. In geo-statistics, interpolation is a method of approximating and assigning new data for locations where no samples have been taken within the range of a discrete set of known data points. There are various interpolation models such like TIN (Triangulated Irregular Network), IDW (Inverse Distance Weighting), Kriging, and natural neighbor, etc.[45]-[48], but which one suits research purpose of farmland terrain best still remains unclear.

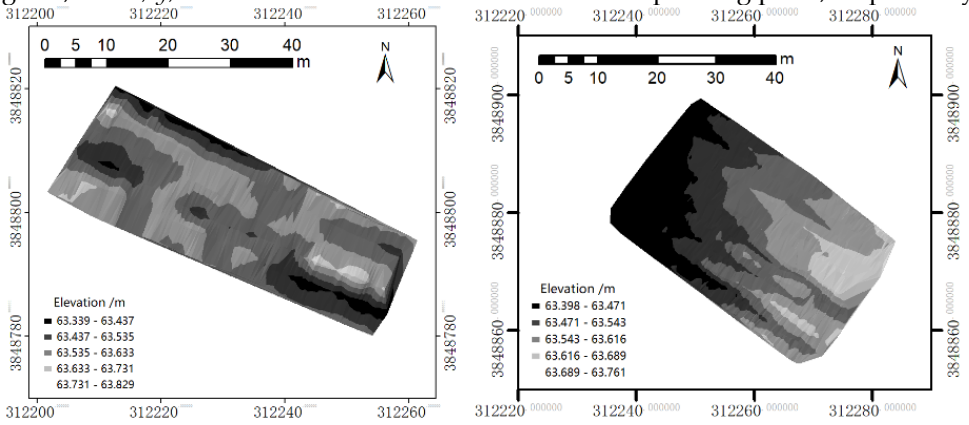
TIN is a vector-based interpolation model, which forms a network of triangles of irregular size and shape. TIN's triangular linear interpolation process begins with determining the triangular to which the interpolation point belongs; then calculating the parameters of *a*, *b*, and *c* for plane equations of each triangular using 3D coordinates of three vertices, expressed as **Equation (9).** The elevation data of every interpolation point within the triangular could be acquired according to **Equation (10)**. In ArcMap software, we

constructed topographic maps to represent the ground elevation features of field 1 and field 2 using TIN model, shown in **Figure 10.** From the maps we may conclude that ground elevation of field 1 varies from 63.339 m to 63.829 m, and distinguishing convex features (ridges) that are shown in bright white color intertwine with concave features (puddles) that are shown in dark black color, with no obvious trend of terrain changing. However, we can visualize a clear low-west-high-east terrain trend for field 2, with the ground elevation changing from 63.398 m to 63.761 m.

$$\begin{bmatrix} z_1 \\ z_2 \\ z_3 \end{bmatrix} = \begin{bmatrix} 1, x_1, y_1 \\ 1, x_2, y_2 \\ 1, x_3, y_3 \end{bmatrix} \begin{bmatrix} a \\ b \\ c \end{bmatrix} \quad (9)$$

$$z = a + bx + cy \quad (10)$$

where a, b, and c is the parameter for determining plane equation; whilst x_i, y_i, and z_i (i=1, 2, and 3) is the 3D coordinate (easting, northing, and elevation) of each vertices of the triangular; and x, y, and z is the 3D coordinates of each interpolating point, respectively.



(a)Field1. (b)Field2.

Figure 10. Topographic maps generated by using TIN interpolating model.

IDW interpolation model assigns a weighted value of serval neighboring points by using an inverse distance weighted technique. The weight parameters could be determined from the mathematical model expressed as **Equation (11)~(13)**. Natural neighbor interpolation model is similar to the IDW model, except that it determines weight parameters by calculating proportionate areas instead of inversed distances. The IDW interpolation result was shown in

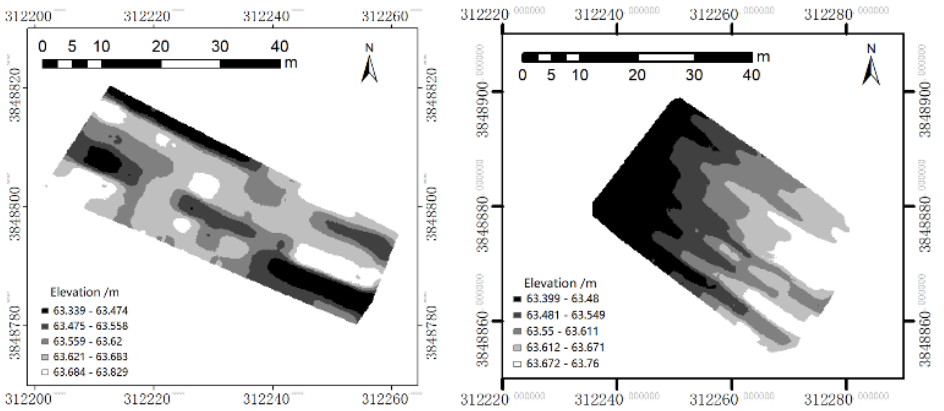
Figure 11, from which we can see more clearly that ridges and puddles spread all around field 1 and the low-west-high-east terrain trend for field 2 is also more obvious, when compared with the topographic maps based on TIN interpolation model. We also created topographic maps using the natural neighbor interpolation model in ArcMap software, shown in **Figure 12**, from which we may observe similar terrain details of the two fields under study when compared with the topographic maps generated by using IDW interpolation model, except that topographic maps based on natural neighbor interpolating model have a more drastic change in ground elevation.

$$w_i = \frac{{d_i}^{-p}}{\sum_{i=1}^{n_{idw}} {d_i}^{-p}} \quad (11)$$

$$d_i = \sqrt{(x - x_i)^2 + (y - y_i)^2} \quad (12)$$

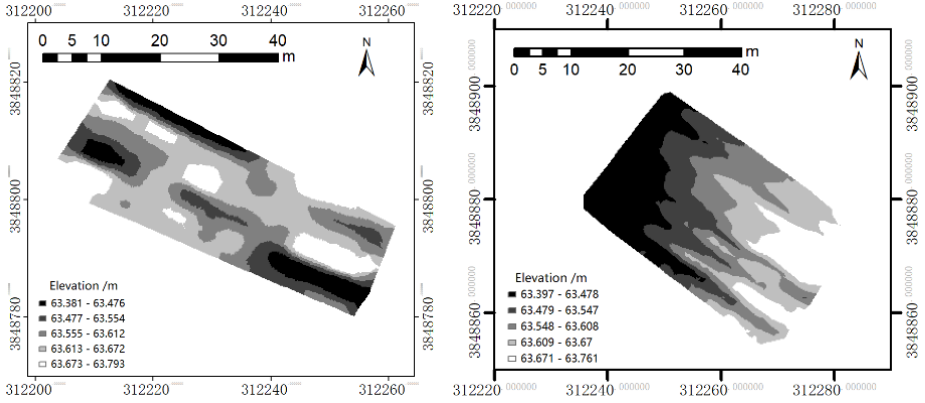
$$\hat{z}(x, y) = \sum_{i=1}^{n_{idw}} w_i z(x_i, y_i) \quad (13)$$

where w_i, d_i, p, and n_{idw} is weighting factor of each measured points, distance of each measured point to interpolating point, power parameter, and number of measured points included in the IDW model, respectively; while (x, y) and (x_i, y_i) is coordinate of easting and northing of interpolating point and each measured point, respectively; $\hat{z}(x, y)$ and $z(x_i, y_i)$ is the estimated ground elevation of the interpolating point and each measured point's ground elevation, respectively.



(a) Field1 (b) Field2

Figure 11. Topographic maps generated by using IDW interpolation model.



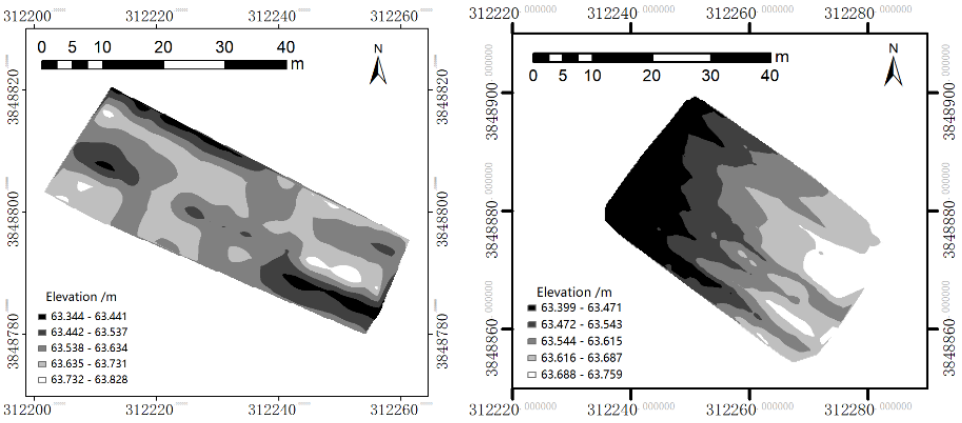
(a) Field1 (b) Field2

Figure 12. Topographic maps generated by using natural neighbor interpolation model.

As mentioned above, TIN, IDW, or natural neighbor interpolation model bases on the surrounding points' z–values for estimating the z–value for each interpolating point. However, Kriging interpolation model incorporates geostatistical relationships among the measured points. Thus, in contrast with IDW model, weight parameter for each surrounding measured point in Kriging interpolation model is not only determined by the inversed distance but also influenced by the overall spatial autocorrelation of the measured points, expressed as **Equation (14)**. In this study we used ordinary Kriging method with spherical semi-variogram model in ArcMap software to generate topographic maps, shown in **Figure 13**, from which we may conclude that the topographic maps based on Kriging interpolation model are quite similar to the topographic maps based on IDW model, and the former are featured with more smooth edges in terms of terrain change.

$$\hat{z}(x,y) = \sum_{i=1}^{n_{kri}} w_i z(x_i, y_i) \quad (14)$$

where $\hat{z}(x,y)$, n_{kri}, w_i, and $z(x_i, y_i)$ is estimated z-value of interpolating point, number of measured points included in Kriging model, weighting factor of each measured points, and each measured point's z -value, respectively.



(a) Field1 (b) Field2

Figure 13. Topographic maps generated by using Kriging interpolation model.

3.3 Evaluating accuracy of UAV-LiDAR topographic mapping system

Table 1 3D coordinates of topographic mapping points measured by UAV-LiDAR topographic mapping system and PPK-GPS module

Field NO.	Point NO.	Easting /m	Northing /m	Ground elevation /m	
				UAV-LiDAR system	Handhold PPK-GPS
Field 1	1	312217.07	3848795.93	63.658	63.616
	2	312217.80	3848801.52	63.628	63.593
	3	312219.74	3848803.24	63.64	63.655
	4	312223.89	3848806.07	63.657	63.679
	5	312226.45	3848809.20	63.649	63.607
	6	312229.30	3848811.51	63.404	63.476
	7	312229.85	3848790.93	63.605	63.565
	8	312233.01	3848793.73	63.67	63.631
	9	312234.60	3848796.05	63.514	63.568
	10	312236.79	3848798.72	63.631	63.664
	11	312239.10	3848802.99	63.572	63.529
	12	312241.29	3848805.18	63.685	63.662
Field 2	1	312243.61	3848872.26	63.420	63.369
	2	312247.92	3848874.06	63.522	63.508
	3	312251.31	3848877.77	63.526	63.509
	4	312254.22	3848881.96	63.531	63.596
	5	312257.82	3848887.05	63.549	63.524
	6	312263.32	3848890.26	63.532	63.584
	7	312273.22	3848883.35	63.609	63.558
	8	312270.82	3848880.46	63.635	63.696

	9	312265.42	3848876.86	63.629	63.542
	10	312262.92	3848873.27	63.641	63.657
	11	312260.31	3848869.36	63.542	63.681
	12	312253.82	3848864.66	63.535	63.578

As indicated in Section 2.2, static positioning accuracy of PPK-GPS module is about 2 cm, which is proved to have high positioning accuracy and could be used as reference data to evaluate the performance of the UAV-LiDAR topographic mapping system. Therefore, we removed the GPS rover receiver from the UAV platform upon the completion of the topographical mapping flight and fixed the antenna of the GPS module onto an aluminum plate. Subsequently, we manually dragged the aluminum plate with GPS antenna over field ground to cross UAV's flight paths, showed in **Figure 1** as green lines. In this way, we acquired accurate 3D coordinates (easting, northing, and elevation) of 12 discrete points distributed around each field, which overlapped (or fell within very near neighborhood of) the topographic mapping points. Geo-spatial coordinates of these points were listed in **Table 1**.

Root Mean Square Error (RMSE) between 12 pairs of ground elevation data of handhold PPK-GPS module and UAV-LiDAR topographic mapping system was calculated as 0.041 m and 0.036 m for field 1 and field 2, respectively, according to **Equation (15)**. RMSE for 2 fields under study showed no significant distinction, although track interval of the UAV-LiDAR topographic mapping system for the 2 fields is quite different (5 m for field 1 and 2.5 m for field 2). Since the ground elevation of the fields under study varies from 63.339 m to 63.829 m and 63.398 m to 63.761 m, respectively, the value of $RMSE_{UAV}$ showed that topographic data of the UAV-LiDAR topographic mapping system are of very high precision.

$$\mathrm{RMSE}_{\mathrm{UAV}} = \sqrt{\frac{\sum_{i=1}^{12}\left(e_{\mathrm{UAVi}} - e_{\mathrm{GPSi}}\right)^2}{12}} \quad (15)$$

where $RMSE_{UAV}$ is the root mean square error between ground elevation data of handhold PPK-GPS module and UAV-LiDAR topographic mapping system; e_{UAVi} and e_{GPSi} indicate the ground elevation data of the UAV-LiDAR topographic mapping system and the handhold PPK-GPS data, respectively.

Accuracy of topographic maps generated by using interpolation models depends on two systems of error. One is accuracy of each measured points, i.e. the primitive error. The other adheres to mathematical model of each specific interpolation model, i.e. the interpolation error. In this study, primitive error is indicated by values of RMSE between ground elevation data of handhold PPK-GPS module and the UAV-LiDAR topographic mapping system, which proved the topographic data of UAV-LiDAR topographic mapping system are very accurate. Interpolation error is the main source that contributes to accuracy of topographic maps, as the z–value of each interpolation point is not only determined by the surrounding points' z–values but also influenced by the neighboring points' spatial distribution.

Table 2 3D coordinates of sampled points acquired by using handhold PPK-GPS module and different interpolation models

Field NO.	Point NO.	Easting /m	Northing /m	Ground elevation /m				
				PPK-GPS	TIN	IDW	Natural Neighbor	Kriging
Field 1	1	312227.81	3848810.62	63.461	63.489	63.476	63.501	63.497
	2	312225.17	3848807.27	63.587	63.657	63.655	63.654	63.654
	3	312222.05	3848804.39	63.693	63.645	63.636	63.632	63.631
	4	312240.04	3848804.39	63.618	63.637	63.644	63.644	63.644
	5	312218.93	3848801.75	63.585	63.636	63.642	63.641	63.643

	6	312238.12	3848800.07	63.656	63.619	63.629	63.617	63.627
	7	312217.25	3848798.15	63.578	63.631	63.642	63.638	63.642
	8	312235.48	3848797.43	63.462	63.570	63.579	63.575	63.577
	9	312234.52	3848795.03	63.704	63.590	63.573	63.585	63.586
	10	312231.64	3848792.63	63.779	63.639	63.636	63.633	63.634
Field 2	1	312259.81	3848887.79	63.589	63.546	63.543	63.546	63.546
	2	312257.09	3848884.10	63.520	63.572	63.581	63.578	63.579
	3	312272.05	3848881.38	63.676	63.626	63.623	63.625	63.624
	4	312253.59	3848879.43	63.554	63.508	63.504	63.502	63.502
	5	312268.75	3848878.85	63.683	63.636	63.626	63.634	63.633
	6	312250.09	3848876.71	63.538	63.481	63.474	63.485	63.483
	7	312264.47	3848874.19	63.670	63.651	63.651	63.652	63.652
	8	312246.78	3848873.41	63.495	63.471	63.462	63.471	63.469
	9	312261.36	3848871.66	63.519	63.578	63.594	63.586	63.588
	10	312256.89	3848867.38	63.593	63.549	63.546	63.549	63.551

In order to evaluate accuracy of topographic maps generated by using different interpolation models, we obtained accurate 3D coordinates of 10 discrete points distributed around each field from the trajectory of handhold PPK-GPS module. Spatial distribution of these evaluating points was also shown as green dots in **Figure 1**, and the 3D coordinates were listed in **Table 2**. Furthermore, according to easting and northing coordinates of handhold PPK-GPS data, the ground elevations of each point in topographic maps of different interpolation models were extracted in ArcMap software and listed in **Table 2**.

Table 3 RMSE between ground elevation data of handhold PPK-GPS module and topographic maps of different interpolating models

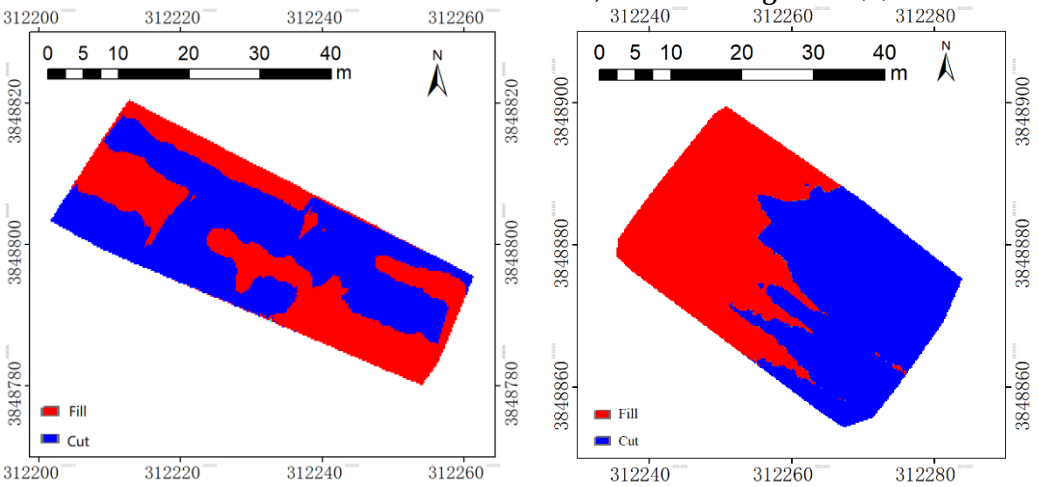
	TIN	IDW	Natural Neighbor	Kriging
Field 1	0.077 m	0.083 m	0.082 m	0.082 m
Field 2	0.046 m	0.053 m	0.048 m	0.049 m

RMSE between ground elevation data of handhold PPK-GPS module and topographic maps of different interpolation models for field 1 and field 2 was calculated, according to **Equation (16)** and listed in **Table 3**. From **Table 3** and $RMSE_{UAV}$ mentioned above, we could conclude that although there is no significant distinction between the primitive error of the UAV-LiDAR topographic mapping system for field 1 and field 2, the difference of interpolating errors among each interpolation model is obvious. TIN interpolation model expressed best performances for both field 1 with sparse topographic surveying points and field 2 with relatively dense topographic surveying points, when compared with other interpolation models like IDW, natural neighbor, and Kriging. Besides, as the spatial resolution of topographic surveying points is improved from 5 m×0.5 m to 2.5 m×0.5 m, the interpolating error of topographic maps based on TIN model drops drastically from 0.077 m to 0.046 m.

$$\mathrm{RMSE}_{\mathrm{map}} = \sqrt{\frac{\sum_{j=1}^{10}\left(e_{\mathrm{mapj}} - e_{\mathrm{GPSj}}\right)^2}{10}} \quad (16)$$

where $RMSE_{map}$ indicates RMSE between the ground elevation data of handhold PPK-GPS and topographic maps of different interpolating models; e_{mapj} and e_{GPSj} indicates ground elevation data of topographic maps using different interpolating models and handhold PPK-GPS module, respectively.

According to the topographic map of TIN models that are most suitable to depict farmland terrains, cut-fill analysis was conducted for each field. Based on statistical results of the ground elevation data from eac topographic maps, average value of each field's ground elevation data was calculated as 63.597 m and 63.564 m. Average value of ground elevation was assigned to new raster models that share same geo-spatial coordinates and resolution with the topographic maps of TIN model as desired ground elevation. By comparing value of ground elevation of each point in the topographic map with the new raster model, operations of cut or fill could be determined, shown in **Figure 14**. Blue color represents the areas where ground elevation is larger than the average value and soils could be cut to form a desired plane, while red color represents the areas where ground elevation is smaller than the average value and it need extra soils to be filled. Furthermore, results of cut-fill analysis showed that for field 1 the volume of cut soil is about 33.2 m^3, which accounted for about 616.4 m^2, showed in **Figure 14 (a)** as blue color; while the areas to be filled with extra soils accounted for about 454.8 m^2, showed in **Figure 14 (a)** as red color. On the other hand, for field 2 the volume of cut soil is about 46.3 m^3, which accounted for about 603.8 m^2, showed in **Figure 14 (b)** as blue color too; and the areas to be filled with extra soils accounted for about 557.6 m^2, showed in **Figure 14 (b)** as red color.



(a) Field 1 (b) Field 2

Figure 14. Cut-fill analysis based on topographic maps of TIN model.

4. Conclusion

In this study, we developed an innovative topographic mapping system by integrating LiDAR distance measurements with PPK GPS coordinates, using a low-altitude UAV as a platform in a simple, efficient, and totally autonomous fashion. The positioning accuracy of PPK- GPS module was experimentally validated as 2 cm, which shows good capability of conducting topographic mapping on farmlands. Topographic mapping experiments in 2 fields were conducted and topographic maps indicating spatial variations of within-field ground elevation were generated. The main conclusions were summarized as follows.

(1). From the topographic maps of graduated symbols, we can understand that ground elevations do not indicate any significant terrain trends for field 1, but 2 concave features (puddles) as well as several convex terrains (ridges) could be clearly observed. On the other hand, the gradual increasing trend in elevation from northwest to southeast end of field 2 is obvious.

(2). RMSE between 12 pairs of ground elevation data of handhold PPK-GPS module and UAV-LiDAR topographic mapping system was calculated as 0.041 m and 0.036 m for field 1 and field 2, respectively. As varying range of ground elevation of field 1 and field

2 is 0.49 m and 0.363 m, respectively, the RMSE showed that topographic data of the UAV-LiDAR topographic mapping system are of high accuracy.

(3). Different interpolation models including TIN, IDW, natural neighbor, and Kriging were used for generating topographic maps based on 675 and 1 626 set of effective topographic mapping data for field 1 and field 2, respectively, so that the most suitable interpolation model could be determined. 3D coordinates of 10 handhold PPK-GPS points as well as corresponding points from each topographic map of different interpolation models were collected around each field under study. From RMSE of ground elevation data, we concluded that there is no significant distinction between primitive error for field 1 and field 2, but the difference of interpolating errors among each interpolation model is obvious.

(4). TIN was proved as the most suitable interpolation model for applications of farmland topographic mapping. Besides, as the spatial resolution of topographic mapping points is improved, the interpolating error of topographic maps based on TIN model drops drastically from 0.077 m to 0.046 m. Cut-fill analysis based on topographic maps of TIN model suggested volumes and areas of soils to be cut or filled, which also provides detailed information on setting height of desired ground plane and path planning of farmland leveler for future study.

Therefore, we can conclude that based on TIN interpolation model, the UAV-LiDAR topographic mapping system could be successfully used to collect topographic data with high accuracy, which are instructive for precision farmland levelling.

Acknowledgements:

This research was jointly funded by The National Key Research and Development Program of China, grant number 2019YFE0125500 and Key Scientific Research Projects of Colleges and Universities in Henan Province, grant number 20A416001.

References

[1]. Hu Lian, Luo Xiwen, et al. Development of 1PJ-4. 0 laser leveler installed on a wheeled tractor for paddy gield. Transactions of the Chinese Society for Agricultural Machinery, 2014,45:146-151. (in Chinese)

[2]. Rickman, J.F., Manual for laser land levelling. Rice-Wheat Consortium Technical Bulletin Series 5, 2002, 110(012):24.

[3]. Liang Z W, Liu X C, Xiao J R, Liu C H. Review of conceptual and systematic progress of precision irrigation. Int J Agric & Biol Eng, 2021; 14(4): 20–31.

[4]. Khalid A A, Abdalhaleem A H, ElKamil T, Ahmed G K, Rangaswamy M, Fahad A, et al. Impacts of center pivot irrigation system uniformity on growth of potato crop and residual soil Nitrogen. Int J Agric & Biol Eng, 2019, 12(1): 126–131.

[5]. Levidow L, Zaccaria D, Maia R, Vivas E, Todorovic M, Scardigno A. Improving water-efficient irrigation: Prospects and difficulties of innovative practices. Agricultural Water Management, 2014,146:84-94.

[6]. Abbaszadeh Shahri, A., Kheiri, A.; Hamzeh, A. Subsurface topographic modeling using geospatial and data driven Algorithm. ISPRS Int. J. Geo-Inf., 2021,10: 341.

[7]. Brandolini, P., Faccini, F., Paliaga, G., Piana, P. Man-made landforms survey and mapping of an urban historical center in a coastal Mediterranean environment. Geogr. Fis. Dinam. Quat. 2018, 41:23–34.

[8]. Gościewski, D.; Gerus Gościewska, M. Adjusting the regular network of squares resolution to the digital terrain model surface shape. ISPRS Int. J. Geo-Inf., 2020, 9: 761.

[9]. Hamid Raeisi Vanani, Mohammad Shayannejad, et al. A simple method for land grading computations and its comparison with genetic algorithm (GA) method. International Journal of Research Studies in Agricultural Sciences, 2017, 3, 8: 26-38.

[10]. Johnson KM, Ouimet WB. Rediscovering the lost archaeological landscape of southern new england using airborne Light Detection and Ranging (LiDAR). Journal of Archaeological Science, 2014, 43:9-20.

[11]. Stroner, M., Urban, R., Seidl, J., Reindl, T., Brouček, J. Photogrammetry using UAV-mounted GNSS RTK: georeferencing strategies without GCPs. Remote Sens. 2021, 13, 1336.

[12]. Remondino F. Heritage recording and 3D modeling with photogrammetry and 3D scanning. Remote Sensing. 2011, 3(6):1104-1138.
[13]. Roncella, R., Bruno, N., Diotri, F., Thoeni, K., Giacomini, A. Photogrammetric digital surface model reconstruction in extreme low-light environments. Remote Sens. 2021, 13, 1261.
[14]. Ping H, Wang J H, Ma Z H, Du Y F. Mini-review of application of IoT technology in monitoring agricultural products quality and safety. Int J Agric & Biol Eng., 2018, 11(5): 35–45.
[15]. Y. Ham, K. K. Han, J. J. Lin, and M. Golparvar-Fard, Visual monitoring of civil infrastructure systems via camera-equipped unmanned aerial vehicles (UAVs): a review of related works. Visualization in Engineering. 2016,4,1.
[16]. Du Mengmeng, Liu Yingchao, Ji Jiangtao, Jin Xin,Zhou Hao, Liu Ke. Farmland topographic mapping based on UAV and LiDAR technology. Transactions of the Chinese Society of Agricultural Engineering, 2020, 36(22): 60-67.(In Chinese)
[17]. Yang, J.; Li, X.; Luo, L.; Zhao, L.; Wei, J.; Ma, T. New Supplementary Photography Methods after the Anomalous of Ground Control Points in UAV Structure-from-Motion Photogrammetry. Drones 2022, 6, 105.
[18]. Resop JP, Hession WC. Terrestrial laser scanning for monitoring streambank retreat: Comparison with traditional surveying techniques. Journal of Hydraulic Engineering. 2010, 136(10):794-8.
[19]. Dardanelli, G., Maltese, A., Pipitone, C., Pisciotta, A., Lo Brutto, M. NRTK, PPP or static, that is the question. Testing different positioning solutions for GNSS survey. Remote Sens. 2021, 13, 1406.
[20]. Keay, S., Earl, G.P., Hay, S., Kay, S., Ogden, J., Strutt, K.D. The role of integrated geophysical survey methods in the assessment of archaeological landscapes: The case of Portus. Archaeol. Prospect. 2009, 16: 154–166.
[21]. Keay, S.J., Parcak, S.H., Strutt, K.D. High resolution space and ground-based remote sensing and implications for landscape archaeology: The case from Portus, Italy. JAS 2014, 52: 277–292.
[22]. Guo Zonghe, Zheng Jinfeng, Cui Yunchuan. Surveying and setting-out based on two-point reference line with total station. Bulletin of Surveying and Mapping, 2004, 8, 22.
[23]. Corsini A, Castagnetti C, Bertacchini E, Rivola R, Ronchetti F, Capra A. Integrating airborne and multi-temporal long-range terrestrial laser scanning with total station measurements for mapping and monitoring a compound slow moving rock slide. Earth surface processes and landforms. 2013, 38(11):1330-1338.
[24]. Rodríguez-Gonzálvez P, Jiménez Fernández-Palacios B, Muñoz-Nieto ÁL, Arias-Sanchez P, Gonzalez-Aguilera D. Mobile LiDAR system: New possibilities for the documentation and dissemination of large cultural heritage sites. Remote Sensing. 2017, 9(3):189.
[25]. Terrone, M., Piana, P., Paliaga, G., D'Orazi, M., Faccini, F. Coupling historical maps and LiDAR data to identify man-made landforms in urban areas. ISPRS Int. J. Geo-Inf. 2021, 10, 349.
[26]. Hirano A, Welch R, Lang H. Mapping from ASTER stereo image data: DEM validation and accuracy assessment. ISPRS Journal of Photogrammetry and Remote Sensing. 2003, 57(5):356-70.
[27]. Doneus, M. Openness as visualization technique for interpretative mapping of airborne Lidar derived digital terrain models. Remote Sens. 2013, 5, 6427–6442.
[28]. Harwin S, Lucieer A. Assessing the accuracy of georeferenced point clouds produced via multi-view stereopsis from un-manned aerial vehicle (UAV) imagery. Remote Sensing. 2012, 4(6):1573-1599.
[29]. Alshawabkeh, Y., Baik, A., Miky, Y. Integration of laser scanner and photogrammetry for heritage BIM enhancement. ISPRS Int. J. Geo-Inf. 2021, 10, 316.
[30]. Lovitt J, Rahman MM, McDermid GJ. Assessing the value of UAV photogrammetry for characterizing terrain in complex peatlands. Remote Sensing. 2017, 9(7):715.
[31]. Jiménez-Jiménez, S.I., Ojeda-Bustamante, W., Marcial-Pablo, M.d.J., Enciso, J. Digital terrain models generated with low-cost UAV photogrammetry: methodology and accuracy. ISPRS Int. J. Geo-Inf. 2021, 10, 285.
[32]. Cho, J.-W.; Lee, J.-K.; Park, J. Large-Scale Earthwork Progress Digitalization Practices Using Series of 3D Models Generated from UAS Images. Drones 2021, 5, 147.
[33]. Crawford, B.; Swanson, E.; Schultz-Fellenz, E.; Collins, A.; Dann, J.; Lathrop, E.; Milazzo, D. A New Method for High Resolution Surface Change Detection: Data Collection and Validation of Measurements from UAS at the Nevada National Security Site, Nevada, USA. Drones 2021, 5, 25.
[34]. D. Angelo, G., Piersanti, M., Pignalberi, A., Coco, I., De Michelis, P., Tozzi, R., Pezzopane, M., Alfonsi, L., Cilliers, P., Ubertini, P. Investigation of the physical processes involved in GNSS amplitude scintillations at high latitude: A case study. Remote Sens. 2021, 13, 2493.
[35]. Liu, X., Chen, H., Jiang, W., Xi, R., Zhao, W., Song, C., Zhou, X. Modeling and assessment of GPS/Galileo/BDS precise point positioning with ambiguity resolution. Remote Sens. 2019, 11, 2693.

[36]. Bewley, R.H., Crutchley, S., Shell, C. New light on an ancient landscape: LiDAR survey in the Stonehenge World Heritage Site. Antiquity 2005, 79, 636–647.
[37]. Devereux, B.J., Amable, G.S., Crow, P. Visualisation of LiDAR terrain models for archaeological feature detection. Antiquity 2008, 82, 470–479.
[38]. Bennett, R., Welham, K., Hill, R.A., Ford, A. A comparison of visualization techniques for models created from airborne laser scanned data. Archaeol. Prospect 2012, 19: 41–48.
[39]. Pricope, N.G.; Minei, A.; Halls, J.N.; Chen, C.; Wang, Y. UAS Hyperspatial LiDAR Data Performance in Delineation and Classification across a Gradient of Wetland Types. Drones 2022, 6, 268.
[40]. Artale V, Milazzo CL, Ricciardello A. Mathematical modeling of hexacopter. Appl. Math. Sci. 2013,7(97):4805-4811.
[41]. Nguyen, D.D.; Rohacs, J.; Rohacs, D. Autonomous flight trajectory control system for drones in smart city traffic management. ISPRS Int. J. Geo-Inf. 2021, 10, 338.
[42]. Zhang J, Ren L, Deng H, Ma M, Zhong X, Wen P. Measurement of unmanned aerial vehicle attitude angles based on a single captured image. Sensors (Basel). 2018,18(8):2655.
[43]. Chiang K.W., Duong T.T., Liao J.K., Lai Y.C., Chang C.C., Cai J.M., Huang S.C. On-Line Smoothing for an integrated navigation system with low-cost MEMS inertial sensors. Sensors. 2012, 12, 17372.
[44]. Zhang J., Yuan H. Analysis of unmanned aerial vehicle navigation and height control system based on GPS. Syst. Eng. Electron. Technol. 2010, 21: 643–649.
[45]. Sun, Y., Zheng, W., Li, Z., Zhou, Z. Improved the accuracy of seafloor topography from altimetry-derived gravity by the topography constraint factor weight optimization method. Remote Sens. 2021, 13, 2277.
[46]. Huang Y. P. Triangular irregular network generation and topographical modeling. Computers in Industry. 1989,12(3):203-213.
[47]. Tsai VJ. Delaunay triangulations in TIN creation: an overview and a linear-time algorithm. International Journal of Geo-graphical Information Science. 1993,7(6):501-524.
[48]. Watson, D. F. and G. M. Philip. A refinement of inverse distance weighted interpolation. Geoprocessing. 1985,2:315–327.